

# Hydrogen embrittlement in micro-architected materials

Danial Molavitabrizi, Haiyang Yu<sup>\*</sup>, S. Mahmoud Mousavi<sup>\*</sup>

Division of Applied Mechanics, Department of Materials Science and Engineering, Uppsala University, 751 03 Uppsala, Sweden

## ARTICLE INFO

### Keywords:

Hydrogen Embrittlement  
Micro-architected materials  
Elastoplastic homogenization  
Degradation law  
Material-property charts

## ABSTRACT

Hydrogen embrittlement is a classical problem in bulk materials while it is rather untouched for advanced materials such as micro-architected materials. This can be a barrier to industrial adoption of these materials where hydrogen is present as a popular source of energy. In this study, we developed a numerical scheme to assess the hydrogen degradation in metallic micro-architected materials. The numerical scheme is built on the concept of elastoplastic homogenization and two hydrogen embrittlement theories, i.e. hydrogen enhanced decohesion (HEDE) and hydrogen enhanced localized plasticity (HELP). The use of homogenization allows for explicit definition of a unit-cell, drastically improving the computation time. The hydrogen degradation loci of two specific micro-architected materials, that is cubic (with 10%, 20% and 30% relative densities) and body-center cubic (with 20% relative density), are numerically characterized. Additionally, the influence of unit-cell topology, relative density, and trap hydrogen on the degradation of homogenized macroscopic material is determined. Finally, a unique failure locus is provided for generic cubic unit-cell with arbitrary relative densities. This degradation law is independent of the relative density and can be interpreted as a material property, contributing to the material design charts.

## 1. Introduction

Micro-architected materials are a class of porous multiscale materials formed by the periodic assembly of a unit-cell (micro to millimeter length-scale) in the design space. The unit-cell architecture can be artificially tailored to achieve a specific property such as negative Poisson's ratio, high acoustic damping, or energy absorption. The porous structure of these materials provides a great weight saving potential. This, in addition to their tailored properties, make micro-architected materials interesting candidates for a wide range of industries. These materials were difficult to fabricate, but the recent advancements in additive manufacturing took this hindrance away and accelerated their industrial adoption. Yet, accurate prediction of the failure and lifetime of these materials is crucial for their wide-spread application.

In this respect, we may classify the literature on micro-architected materials into two groups. Some studies focus on the conceptual design and physics governing the behavior of these materials, e.g. [1], [2], [3], [4], [5] and [6], while others investigate the failure (quasi-static and fatigue) under compression, e.g. [7], [8], [9], [10] and [11], and (more recently) under tension, e.g. [12], [13], [14], [15], [16] and [17]. Most of these failure-related studies highlighted the role of manufacturing imperfections, and some thoroughly investigated the topic, e.g. see [8], [9], [14] and [16]. These imperfections (like void, strut waviness and surface

<sup>\*</sup> Corresponding authors.

E-mail addresses: [danial.molavitabrizi@angstrom.uu.se](mailto:danial.molavitabrizi@angstrom.uu.se) (D. Molavitabrizi), [haiyang.yu@angstrom.uu.se](mailto:haiyang.yu@angstrom.uu.se) (H. Yu), [mahmoud.mousavi@angstrom.uu.se](mailto:mahmoud.mousavi@angstrom.uu.se) (S. Mahmoud Mousavi).

<https://doi.org/10.1016/j.engfracmech.2022.108762>

Received 27 June 2022; Received in revised form 6 August 2022; Accepted 28 August 2022

Available online 9 September 2022

0013-7944/© 2022 The Author(s). Published by Elsevier Ltd. This is an open access article under the CC BY license (<http://creativecommons.org/licenses/by/4.0/>).

roughness) often arise from additive manufacturing processes, and noticeably influence the material behavior. This topic has gained attention, and some recent studies are solely devoted to the analysis of defects in micro-architected materials, e.g. [18], [19], [20] and [21].

We argue that additive manufacturing defects are not the only imperfections that a micro-architected material may encounter. As we move towards a more sustainable future, fossil fuels are being replaced by alternative sources of energy. Hydrogen is one of the main alternatives, especially in aerospace and automotive industry. These industries employ micro-architected materials in their products, potentially facing a new challenge, that is hydrogen embrittlement in metallic micro-architected materials. To the authors' knowledge, this form of defect in micro-architected materials has not been addressed in the literature.

Hydrogen embrittlement is a well-known issue in bulk metallic materials, which has been studied both numerically, e.g. [22], [23], [24] and [25], and experimentally, e.g. [26] and [27]. More recently, the research on this topic has extended to additively manufactured bulk materials, e.g. see [28], [29] and [30]. There exist two prevailing theories for hydrogen embrittlement, namely the hydrogen enhanced decohesion (HEDE) mechanism and the hydrogen enhanced localized plasticity (HELP) mechanism. The former assumes that hydrogen reduces the cohesive strength of material lattice, and the latter assumes that hydrogen enhances dislocation activity, leading to localized plasticity and reduced global plastic flow. So far, it is still unclear how the presence of hydrogen affects the macroscopic behaviour of micro-architected materials. In this study, we address this question.

To capture hydrogen embrittlement in micro-architected materials, we develop a computational framework with explicit definition of material unit-cell with periodic boundary conditions (PBC). We combine this model with hydrogen diffusion equations and update the materials flow and maximum stress based on the HEDE and HELP mechanisms. We then use elastoplastic homogenization to compute the macroscopic material behavior. The developed model is generic and applicable to any arbitrary micro-architected material.

We organize the paper as follow. In Section 2, we derive the governing equations for hydrogen diffusion, discuss how hydrogen concentration affects material's constitutive behavior, and review elastoplastic homogenization theory. We then calibrate the material model and elaborate on the numerical scheme and its implementation in Sections 3 and 4, respectively. In Section 5, we apply the model to two micro-architected materials, namely cubic and body-centered cubic (BCC), to characterize their macroscopic hydrogen degradation laws. We also investigate the influence of relative density, unit-cell architecture (topology) and trap hydrogen on strength degradation of the candidate materials. Finally, we conclude on the results and provide suggestions in Section 6.

## 2. Theory and method

In this section, we follow a coupled chemo-mechanical analysis and derive the governing equations for hydrogen diffusion under quasi-static loading conditions. We then elaborate on Orian's theory to determine trap hydrogen concentration. The influence of hydrogen on mechanical properties, the flow stress and failure criterion are then introduced. Finally, we review the concepts behind elastoplastic homogenization for the analysis of multiscale materials.

### 2.1. Hydrogen diffusion

We start formulating the diffusion problem for the most general case using Reynold's transport theorem. For a continuum body  $\Omega$  in spatial frame, this reads as.

$$\frac{D}{Dt} \int_{\Omega} \varphi dv = \int_{\partial\Omega} f \cdot \mathbf{n} ds + \int_{\Omega} \frac{\partial \varphi}{\partial t} dv \quad (1)$$

Here,  $\varphi(x, t)$  is a spatial scalar field per unit volume,  $\frac{D}{Dt}$  is material time derivative,  $\frac{\partial}{\partial t}$  is spatial time derivative,  $f$  is the flux acting on the boundary surface  $\partial\Omega$ , and  $\mathbf{n}$  is the outward unit normal of this surface. The scalar field  $\varphi$  defines a physical quantity. Hydrogen diffusion is a mass transport phenomenon, and here we consider  $\varphi$  to be the total hydrogen concentration, i.e.  $C_{tot} = C_L + C_T$ . The concentration  $C_L$  denotes the hydrogen concentration at normal interstitial lattice sites (NILS) and  $C_T$  denotes the hydrogen concentration trapped at dislocations, grain boundaries and second phase interfaces. With this, Eq. (1) becomes.

$$\frac{D}{Dt} \int_{\Omega} C_{tot} dv = \int_{\partial\Omega} \mathbf{J} \cdot \mathbf{n} ds + \int_{\Omega} \frac{\partial C_{tot}}{\partial t} dv \quad (2)$$

where,  $\mathbf{J}$  is the hydrogen flux through surface  $\partial\Omega$ . The driving force for hydrogen diffusion is the gradient in chemical potential,  $\nabla\mu$ , and thus, the flux is defined as [23].

$$\mathbf{J} = -\frac{D_L C_L}{RT} \nabla\mu \quad (3)$$

where,  $D_L$  is diffusion coefficient,  $R$  is gas constant, and  $T$  is the temperature. Bridging the chemistry and mechanics, the chemical potential at an arbitrary point reads, [22] and [23],

$$\mu = \mu_0 + RT \ln(C_L) - V_H \sigma_H \quad (4)$$

Here,  $\mu_0$  is the chemical potential at standard state,  $\sigma_H$  is the hydrostatic stress, and  $V_H$  is the partial molar volume of hydrogen.

Considering the conservation of mass and substituting Eqs. (3) and (4) into (2) we have.

$$\int_{\partial\Omega} -\frac{D_L C_L}{RT} [RT\nabla(\ln C_L) - V_H \nabla \sigma_H] \cdot \mathbf{n} ds + \int_{\Omega} \frac{\partial C_{tot}}{\partial t} dv = 0 \quad (5)$$

Using divergence theorem, this converts to.

$$\int_{\partial\Omega} \nabla \cdot \left[ \frac{V_H D_L C_L}{RT} \nabla \sigma_H - D_L C_L \nabla(\ln C_L) \right] dv + \int_{\Omega} \frac{\partial C_{tot}}{\partial t} dv = 0 \quad (6)$$

Under quasi-static loading at sufficiently low rates in which hydrogen equilibrium is maintained, the second integral on the left-hand side vanishes, resulting in.

$$\nabla \left( \frac{V_H}{RT} \sigma_H - \ln C_L \right) = 0 \quad (7)$$

Since both  $\sigma_H$  and  $C_L$  are functions of space, we conclude.

$$\ln C_L = \frac{V_H}{RT} \sigma_H \quad (8)$$

The above equation is valid for a material point at time  $t$ . We may write this equation for another point at far field (i.e. the reference point far from stress concentration) as.

$$\ln C_L^\infty = \frac{V_H}{RT} \sigma_H^\infty \quad (9)$$

where,  $C_L^\infty$  and  $\sigma_H^\infty$  are NILS hydrogen concentration and hydrostatic stress at far field. Subtracting Eq. (9) from (10) yields.

$$C_L = C_L^\infty \exp\left(\frac{V_H}{RT} (\sigma_H - \sigma_H^\infty)\right) \quad (10)$$

This is the equation we use to evaluate NILS hydrogen concentration. With this information at hand, we then determine the concentration of trap hydrogen using Oriani's theory [31] in the next section.

## 2.2. Trapped hydrogen and Oriani theory

We begin by defining the hydrogen concentration at NILS and trap sites, respectively, as.

$$C_L = \beta \theta_L N_L \quad (11)$$

$$C_T = \alpha \theta_T N_T \quad (12)$$

where,  $\theta_L$  is the fraction of occupied NILS sites,  $\beta$  is the number of NILS per lattice atom, and  $N_L$  is the number of lattice atoms per unit volume. Similarly,  $\theta_T$  is the fraction of occupied trap sites,  $\alpha$  is the number of atom sites per trap and  $N_T$  is the number of traps per unit volume. Oriani [31] assumes an equilibrium between occupancy of NILS and trap hydrogen as.

$$\frac{\theta_T}{1 - \theta_T} = K \frac{\theta_L}{1 - \theta_L} \quad (13)$$

where,  $K$  is a constant related to hydrogen binding energy,  $\Delta H$ , defined as  $K = \exp\left(-\frac{\Delta H}{RT}\right)$ . Since  $\theta_L \ll 1$ , the above equation simplifies to.

$$\theta_T = \frac{K \theta_L}{1 + K \theta_L} = \frac{K C_L}{\beta C_L + K C_L} \quad (14)$$

Here, we only consider the hydrogen trapped at dislocations and exclude the ones trapped at grain boundaries and/or second phase interfaces. These (excluded traps) are often referred to as "irreversible traps" due to their high binding energies (high absolute  $\Delta H$  values) which eliminate them from diffusion process. Under this assumption,  $N_T$  in Eq. (12) is a function of dislocation density,  $\rho_d$ , which reads as [22].

$$N_T = \frac{\sqrt{2} \rho_d}{a} \quad (15)$$

where,  $a$  is lattice parameter. Moreover, the dislocation density increases with equivalent plastic strain as.

$$\rho_d = \begin{cases} \rho_0 + k_1 \varepsilon^p & \varepsilon^p \leq 0.5 \\ k_2 \varepsilon^p & \varepsilon^p > 0.5 \end{cases} \quad (16)$$

Here,  $\rho_0$  is the dislocation density of the material at zero plastic strain, and  $k_1$  and  $k_2$  are material constants. We obtain the trap hydrogen concentration using the value of  $C_L$  from Eq. (10) along with Eqs. (12)–(16).

### 2.3. Constitutive model

The total hydrogen concentration affects the plastic behaviour of the host material. The HELP mechanism states that the material flow stress,  $\sigma_f$ , decreases with an increase in hydrogen concentration, e.g. [32], [33] and [34], as.

$$\sigma_f(C_{tot}, \varepsilon^p) = \sigma_o(C_{tot}) \left(1 + \frac{\varepsilon^p}{\varepsilon_o}\right)^N \quad (17)$$

in which,  $\sigma_o(C_{tot})$  is the initial yield stress in presence of hydrogen,  $N$  is the hardening exponent,  $\varepsilon^p$  is the equivalent plastic strain, and  $\varepsilon_o = \sigma_o/E$  with  $E$  and  $\sigma_o$  being the elastic modulus and initial yield stress in the absence of hydrogen, respectively. Here, we follow [25] and evaluate  $\sigma_o(C_{tot})$  as.

$$\sigma_o(C_{tot}) = \begin{cases} \left[ (\xi - 1) \frac{C_{tot}}{C_0} + 1 \right] \sigma_o & \text{for } \sigma_o(C_{tot}) > \psi \sigma_o \\ \psi \sigma_o & \text{for } \sigma_o(C_{tot}) \leq \psi \sigma_o \end{cases} \quad (18)$$

where,  $\xi \leq 1$  is a softening parameter,  $\psi \sigma_o$  is the lowest value of the yield stress with  $\psi$  being a dimensionless parameter varying from 0 to 1, and  $C_0 = 1$  is the reference concentration used to make the equation dimensionally consistent.

Hydrogen concentration also affects the ultimate tensile strength of the material. We formulate this (for AISI 4135) as [24].

$$\sigma_{ut}(C_{tot}) = \sigma_{ut,o} (0.421 \exp(-2.227 C_L) + 0.579) \quad (19)$$

with  $\sigma_{ut,o}$  being the initial ultimate tensile strength of the material in absence of hydrogen.

### 2.4. Homogenization

The theories discussed in Sections 2.1–2.3 describe the behavior of a homogeneous solid material. To assess the behavior of a multiscale material, we need to bridge between scales, i.e. from microscale to macroscale, using homogenization. Periodic micro-architected materials are formed by the tessellation of a unit-cell in the design space. We investigate the behavior of these materials by isolating a single unit-cell, also referred to as a representative volume element (RVE), subjected to periodic boundary condition (PBC). We then take the volume average of microscopic fields over the RVE domain to obtain the effective material properties. This approach is referred to as ‘‘averaging homogenization’’, and is well-established for the analysis of multi-scale materials, e.g. see [35], [36] and [4] for more details.

We assume the strain field is composed of a constant macroscopic strain,  $\bar{\varepsilon}$ , and a microscopic (fluctuation) strain,  $\varepsilon^*$ , that is  $\varepsilon = \bar{\varepsilon} + \varepsilon^*$  (where microscopic strain tensor is the symmetric part of gradient of microscopic displacements,  $u^*$ ). The application of PBC guarantees that the microscopic displacements are equal at any two analogous points located on the opposite sides of an RVE. For instance, if nodes  $A$  and  $B$  are on two opposite sides, the PBC constraints the nodes such that  $u_A^* = u_B^*$ .

Under the stated conditions, we derive the effective elastic properties of a heterogenous material by applying six macroscopic strain states as follow.

$$\bar{\varepsilon}^{(ij)} = \frac{1}{2} \left( (e_i \otimes e_j) + (e_j \otimes e_i)^T \right) \quad (20)$$

where,  $e_i$  ( $i = 1, 2, 3$ ) are the unit basis vectors. We then obtain the material macroscopic stress,  $\bar{\sigma}$ , by taking the volume average of the resulting stress field over the RVE. This, expressed in Voigt’s notation for computational implementation, reads as.

$$[\bar{\sigma}] = \frac{1}{V_{RVE}} \int_{\Omega_{RVE}} [\sigma_{(x)}] dV \quad (21)$$

in which  $\Omega_{RVE}$  defines the RVE domain. Considering Hooke’s law for a homogenous linear elastic material, we have.

$$[\bar{\sigma}] = [C][\bar{\varepsilon}] \quad (22)$$

where,  $[C]$  is the effective elasticity matrix of the homogenized material. In the presence of plasticity and under the assumption of small strains, we additively decompose the macroscopic strain field into elastic and plastic parts, i.e.  $[\bar{\varepsilon}] = [\bar{\varepsilon}^e] + [\bar{\varepsilon}^p]$ . Consequently.

$$[\bar{\sigma}] = [C][\bar{\varepsilon}^e] = [C]([\bar{\varepsilon}] - [\bar{\varepsilon}^p]) \quad (23)$$

In the following, we use the theories elaborated in this section as tools to construct a numerical scheme and study the hydrogen embrittlement in micro-architected materials.

### 3. Material calibration

To analyze the influence of hydrogen on micro-architected materials, we first need to determine the properties of the base material. We choose AISI 4135 (B-15) steel as the base material, for which we have experimental and numerical data on its hydrogen-charged tensile specimens in the literature, e.g. [22] and [27]. Using the available data, we calibrated the material’s true stress–strain

**Table 1**  
Mechanical properties of AISI 4135 in absence of hydrogen.

Elastic modulus ( $E$ )	Yield stress ( $\sigma_0$ )	Hardening exponent ( $N$ )	Ultimate tensile strain ( $\epsilon_{ut}$ )
195 GPa	1320 MPa	0.11	1.7 %

**Table 2**  
Material parameters for hydrogen diffusion in AISI 4135.

Number of trap sites per lattice atom ( $\alpha$ )	1
Number of NIS sites per lattice atom ( $\beta$ )	6
Dislocation density at zero plastic strain ( $\rho_0$ )	$10 \times 10^{-10} m^{-2}$
Lattice Parameter ( $a$ )	$2.86 \times 10^{-10} m$
Hydrogen binding energy ( $\Delta H$ )	$-18 KJ.mol^{-1}$
Number of lattice atoms per volume ( $N_L$ )	$8.64 \times 10^{28} m^{-3}$
Partial molar volume of hydrogen ( $V_H$ )	$2 \times 10^{-6} m^3.mol^{-1}$
Parameters related to dislocation density	$k_1 = 2 \times 10^{16} m^{-2}, k_2 = 10^{16} m^{-2}$

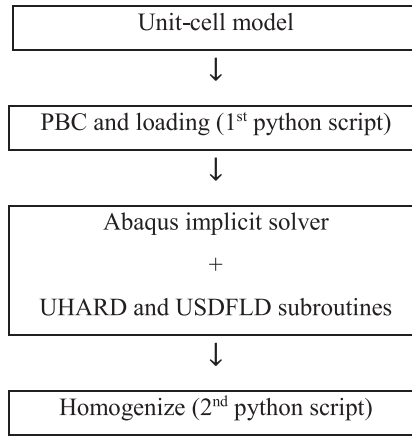


**Fig. 1.** Overview of the numerical scheme.

response in the absence of hydrogen ( $C_{tot} = 0$ ) in the form of Eq. (17), see Table 1. However, the material properties listed in Table 1 are insufficient for calibration of the material failure because notch radius and consequently stress triaxiality affect the maximum strength of the sample.

Within fracture community, it is common to characterize the material failure in terms of plastic strain and stress triaxiality, e.g. see [37], [38] and [39]. Such relations are not explicitly provided when the measure is the maximum strength, while most studies on hydrogen embrittlement use stress-based criteria in their analyses, e.g. [22], [24], [27] and [25]. For that, we employ the failure strength data in [22] and perform numerical simulations on notched tensile specimens (see Appendix A) to characterize the failure locus of the material in terms of maximum strength and stress triaxiality. We record the applied displacement and reaction force at each time increment of the numerical test, and divide them, respectively, by initial length and cross-sectional area at the center of the specimen to obtain the nominal stress–strain curve. We stop the simulation once the maximum global stress (according to provided experimental data in [22]) is reached, and store the local stress and stress triaxiality of the element with maximum principal stress at the vicinity of notch. We use this data to fit an expression and relate the maximum (ultimate tensile) strength in the absence of hydrogen  $\sigma_{ut,0}$  with stress triaxiality  $\eta$  as.

$$\sigma_{ut,0} = 2600\eta^{0.47} \quad (24)$$

This expression is used as an input for Eq. (19) to include the effect of notch.

Finally, we summarize other material parameters required for the simulation of hydrogen diffusion in AISI 4135 [22] in Table 2. We assume the tests are conducted at room temperature. Also, note that the reported hydrogen binding energy is the lower limit of the range provided in [22]. This is because we only considered dislocation traps, excluding traps at grain boundaries, carbides, etc. Yet, the given material parameters only serve as a case study and can be easily modified in the developed framework (see Section 4).

#### 4. Numerical implementation

The hydrogen degradation models (Section 2) have been previously implement in finite element software to study the phenomenon

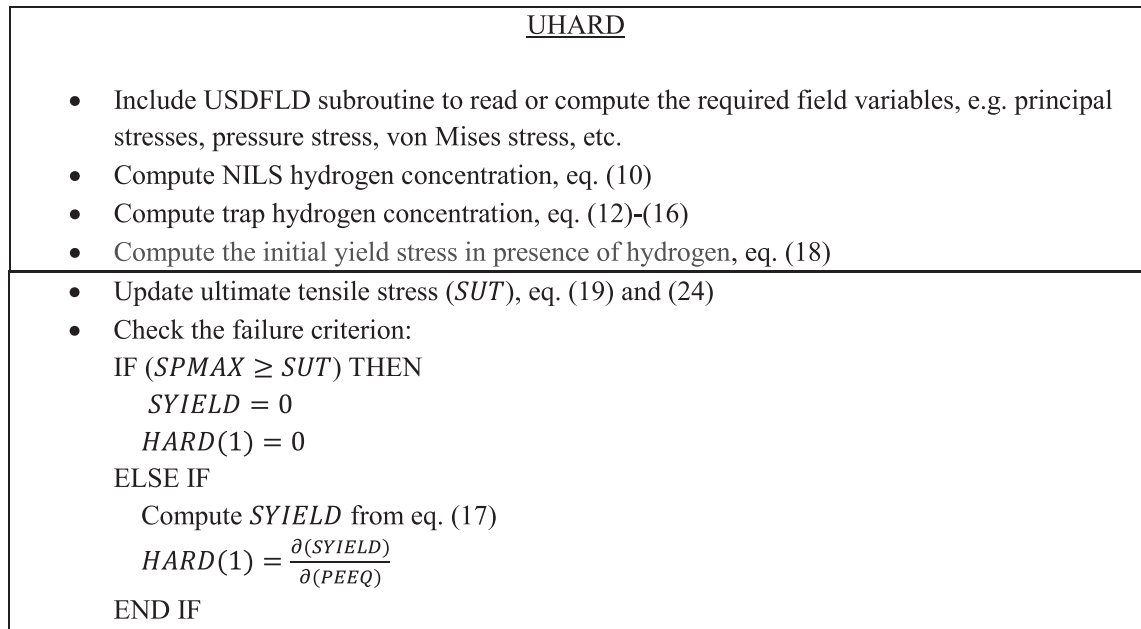


Fig. 2. Algorithm for UHARD subroutine.

in bulk materials, e.g. see [23], [24], [25] and [40]. Here, we make connection between theories reviewed in Section 2 and develop an integrated numerical scheme for the analysis of hydrogen embrittlement in micro-architected materials. We execute coupled chemo-mechanical analysis under quasi-static loading, in which the mechanical homogenization is updated with the input from implicit diffusion equations. The overall simulation process is shown in Fig. 1. We first discuss the general procedure, and then explain the subroutines for hydrogen embrittlement (UHARD and USDFLD) in more detail. The details of elastoplastic homogenization scheme (1st and 2nd python script in Fig. 1) are provided in [16], and we skip further explanation here.

We simulate uniaxial strain-controlled tensile tests by applying macroscopic strains to the material unit-cell with PBC. We then pass the model to Abaqus 2019 implicit solvers along with two Fortran subroutines, i.e. UHARD and USDFLD. We use UHARD to define hydrogen concentration (Sections 2.1 and 2.2), update the flow stress with the progression of hydrogen (Section 2.3), and revise the value of maximum stress with respect to stress triaxiality (calibrated in Section 3). We also need to employ USDFLD to access field variables at material points during the analysis. Once the simulation is complete, we read the output data and perform averaging according to elastoplastic homogenization rules (Section 2.4) using another python script.

We illustrate the structure of UHARD subroutine in Fig. 2. We start by computing and/or reading the field variables in USDFLD. We then proceed with the UHARD code, for which we should define the flow stress, *SYIELD*, and variation of flow stress with respect to equivalent plastic strain, *PEEQ*, that is  $HARD(1) = \frac{\partial(SYIELD)}{\partial(PEEQ)}$  (suppose the flow stress is independent of strain rate and temperature). For that, we first calculate the values of NILS and trap hydrogen concentrations, and then use that as input to Eq. (18) to obtain the initial yield stress in the presence of hydrogen. Next, we determine the value of ultimate tensile stress for each material point considering its stress triaxiality using Eqs. (23) and (24). Eventually, we check the failure criterion in which a material point fails when the value of maximum principal stress, *SPMAX*, exceeds the value of ultimate stress, *SUT*, at that point. If failure occurs, we set the value of flow stress and *HARD*(1) equal to zero. Otherwise, we follow Eq. (17) to update the flow stress and compute *HARD*(1) accordingly.

Note that we discard the post-failure behavior and carry out the simulation until just before the macroscopic stress drops. In fact, we report the material's maximum stress (ultimate tensile stress) as a measure for assessment of hydrogen embrittlement.

## 5. Results and discussion

We study the mechanical response of hydrogen pre-charged micro-architected materials under macroscopic tensile loads using the numerical code. We assume the pre-charging time has been sufficient to have a spatially uniform hydrogen concentration over the unit-cell, which is reasonable for high strength steel with a large hydrogen diffusion coefficient. This is especially the case for open-cell micro-architected materials, where the bulk material is immersed in the hydrogen environment. Yet, additively manufactured micro-architectures may have defects (for example residual stresses at unit-cell joints), which can influence the initial hydrogen distribution. But the presence and severity of such defects are subjective to the choice of additive manufacturing method and its processing parameters. Thus, we exclude these defects and assume to have perfectly fabricated materials.

We start the analysis with the total hydrogen concentration, i.e. both NILS and trap hydrogen, to evaluate whether the trap hydrogen affects the material behavior or not. Next, as a case study, we implement the numerical scheme on cubic unit-cell and characterize its mechanical performance in the presence of hydrogen. Finally, we implement the code on other unit-cell topologies to

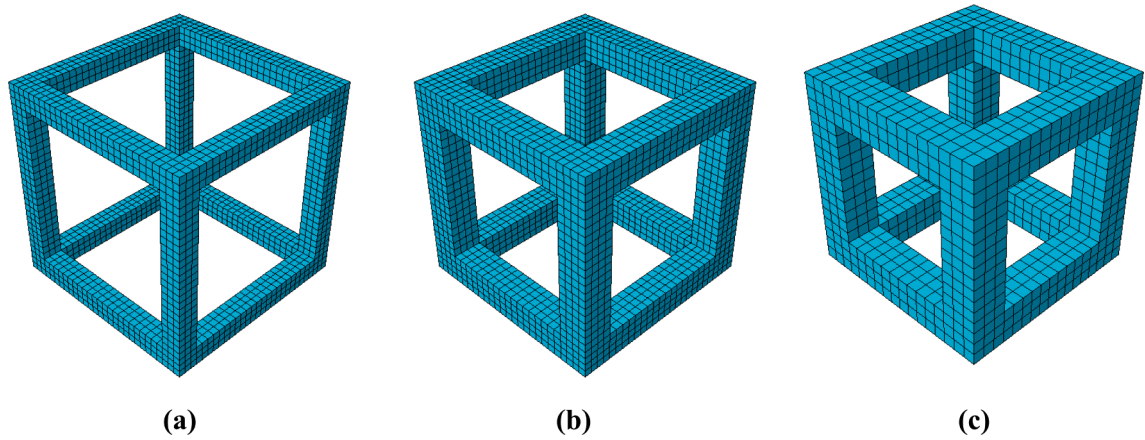


Fig. 3. Cubic unit-cell with: (a)  $\rho_r = 10\%$ , (b)  $\rho_r = 20\%$ , and (c)  $\rho_r = 30\%$ .

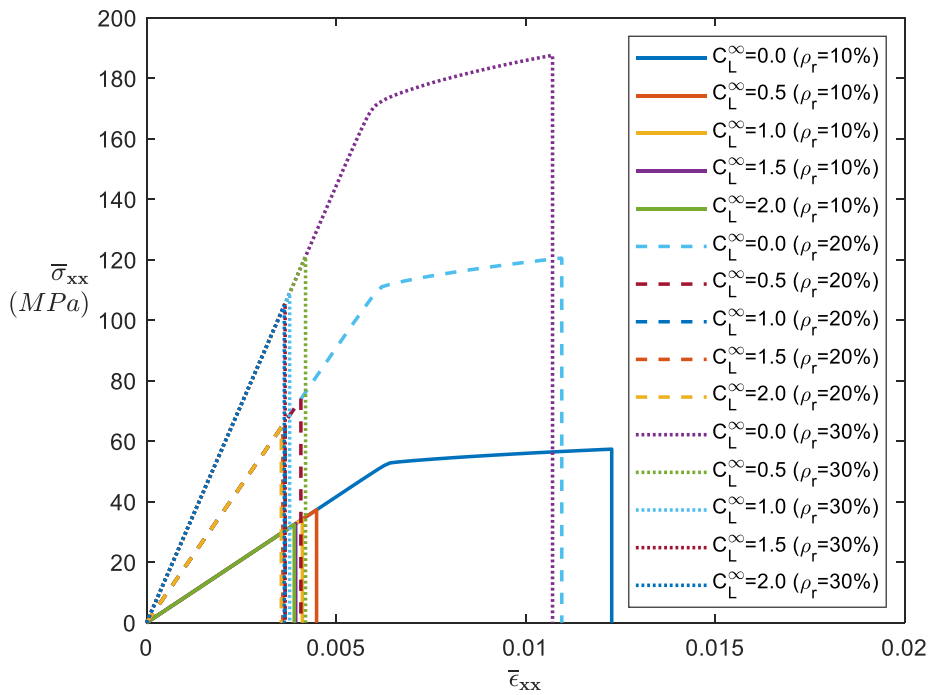


Fig. 4. Macroscopic stress–strain curves for cubic unit-cell with various relative densities ( $\rho_r$ ) and initial hydrogen concentrations ( $C_L^\infty$ ). Plots for  $\rho_r = 10\%$ ,  $\rho_r = 20\%$  and  $\rho_r = 30\%$  are represented with solid, dashed, and dotted lines, respectively. (For colors, refer to online version).

examine the role of unit-cell architecture.

### 5.1. Influence of trap hydrogen

To assess the influence of trap hydrogen on maximum strength in micro-architected materials, we ran simulations under two conditions: (1)  $C_{tot} = C_L$ , and (2)  $C_{tot} = C_L + C_T$ . We noticed the results barely change in the presence of trap hydrogen. In fact, the low ductility of the base material (high-strength steel, AISI 4135) prohibits large scale plasticity. This is even more dominant in micro-architected materials, as they often have lower ductility compared to their base material. Especially in the presence of hydrogen, little to no plasticity develops before the failure of micro-architected materials made of AISI 4135. This makes the contribution of trap hydrogen in the fracture process negligible. However, the situation may differ if we chose a more ductile metal, e.g. low- or mid-strength steel, as the base material. In that case, the concentration of trap hydrogen, especially reversible traps, may influence the process of crack initiation and propagation. Yet, our conclusion about micro-architected materials agrees with what Ayas et al. [22] claimed about the bulk samples made of high-strength steel.

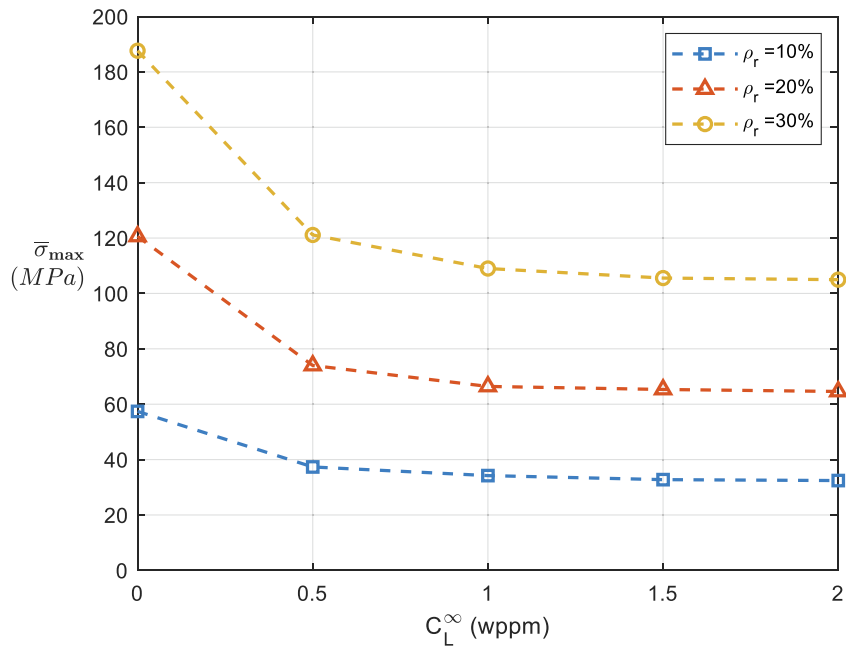


Fig. 5. Macroscopic maximum stress versus pre-charged hydrogen concentration.

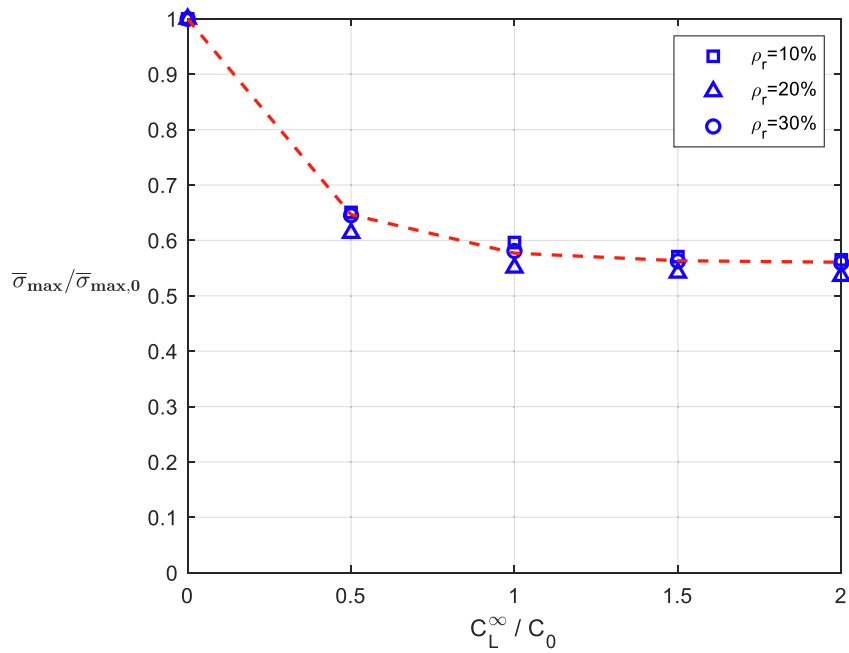


Fig. 6. Normalized failures locus of the cubic unit-cell made of AISI 4135 ( $C_0 = 1wppm$ ).

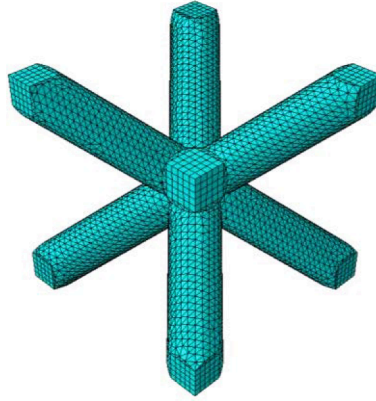


Fig. 7. BCC unit-cell with  $\rho_r = 20\%$ .

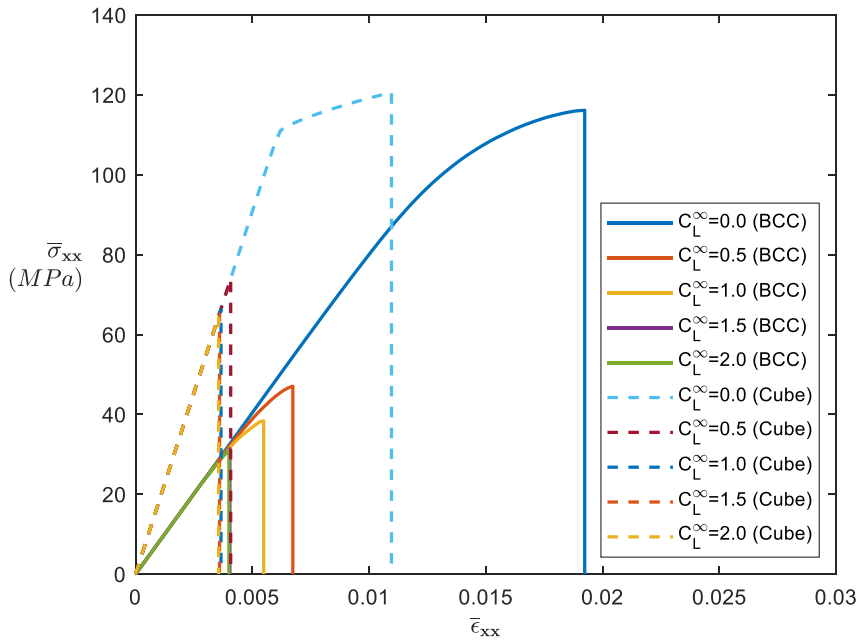


Fig. 8. Macroscopic stress–strain curves for cubic and BCC cells ( $\rho_r = 20\%$ ) at different pre-charged hydrogen concentrations. Plots for BCC and cubic cells are represented with solid and dashed lines, respectively. (For colors, refer to online version.).

In the following, we provide the results based on NILS concentration,  $C_{tot} = C_L$ , as the contribution of trap hydrogen in total concentration,  $C_{tot} = C_L + C_T$ , is negligible for the base material considered here.

## 5.2. Cubic unit-cell

As a case study, we apply the developed model to a micro-architected material with cubic unit-cell made of AISI 4135 steel. This cell topology is stiff and strong when loaded in axial directions, and thus, is a potential candidate for load bearing applications. We characterize hydrogen embrittlement in cubic unit-cells for a range of relative densities,  $\rho_r$  (i.e. volume of solid material divided by unit-cell volume). We design unit-cells with 5 mm cell length. The unit-cell struts have square cross-section with diameters of 1.4 mm ( $\rho_r = 10\%$ ), 2.0 mm ( $\rho_r = 20\%$ ) and 2.5 mm ( $\rho_r = 30\%$ ), see Fig. 3. We mesh the unit-cells with 8-node linear brick elements and set the element size as 1/8th of strut diameter.

We use the numerical code to apply a uniaxial macroscopic strain and obtain the homogenized stress–strain curves for different pre-charge hydrogen concentration values, see Fig. 4. We may draw the following conclusions from the homogenized fields depicted in the

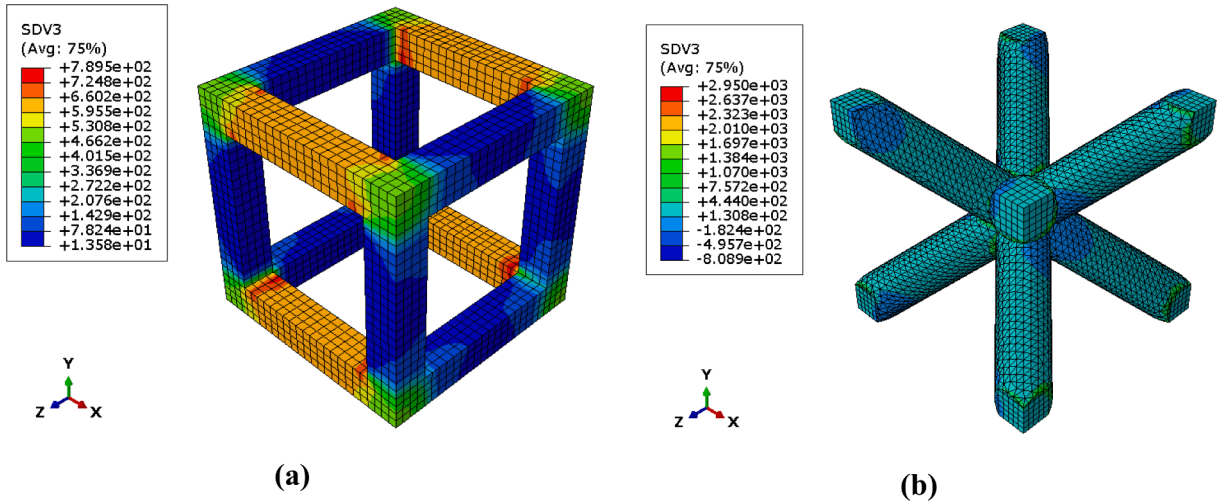


Fig. 9. Maximum principal stress (SVD3) distribution in (a) cubic, (b) BCC cells with  $\rho_r = 20\%$ . The applied macroscopic load for both cases is  $\bar{\epsilon}_{xx} = 0.3\%$ .

plot:

- At a given pre-charge concentration  $C_L^\infty$ , the unit-cells with higher density have considerably higher maximum strength, and slightly lower ductility compared to cells with lower density. For instance, at  $C_L^\infty = 0$ , the cell with  $\rho_r = 20\%$  has 8 % lower ductility and 110 % higher maximum strength compared to the cell with  $\rho_r = 10\%$ .
- The presence of hydrogen noticeably reduces the maximum strength and ductility of the material. This is true for all unit-cells with various relative densities. When the base material has low ductility, e.g. high strength-steel, the presence of hydrogen may change the behavior of micro-architected material from ductile to brittle.

We use the homogenized material response to build a failure locus for cubic material in the space of maximum macroscopic stress,  $\bar{\sigma}_{max}$ , and pre-charge hydrogen concentration, see Fig. 5. The maximum macroscopic strength of the material declines as pre-charged hydrogen concentration increases. This trend follows until material reaches  $C_L^\infty = 1$ , at which a further increase in hydrogen concentration does not affect the maximum strength levels. We shall refer to this point as saturation point.

We then normalize the three failure loci by dividing each curve by its maximum macroscopic strength in the absence of hydrogen,  $\bar{\sigma}_{max,0}$ . Fig. 6 shows the normalized data points fall on a single curve. Thus, instead of using separate failure loci, we introduce one unique expression to characterize the hydrogen embrittlement in cubic unit-cell as.

$$\frac{\bar{\sigma}_{max}}{\bar{\sigma}_{max,0}} = 0.44\exp(-3.25C_L^\infty) + 0.56 \quad (25)$$

where,  $\bar{\sigma}_{max}$  is the maximum macroscopic strength of the cubic material in the presence of hydrogen. We can interpret this as a material property for the cubic micro-architecture material being independent of relative density. This outcome could be of great interest to the engineering community, as it contributes to the material property charts, e.g. see [1].

### 5.3. Role of unit-cell topology

We characterized the failure locus for cubic unit-cell and obtained a single failure locus for a range of relative densities. Yet, the question remains whether the cell topology affects the material behavior or not. We investigate this by applying the numerical scheme to another unit-cell known as body-centered cubic (BCC) made of AISI 4135, see Fig. 7.

We design the unit-cell with  $\rho_r = 20\%$  and 5 mm cell length. The unit-cell struts have circular cross-section with diameters of 1.075 mm. We discretize the model using both quadratic tetrahedral and brick elements with the element size of 1/8th of strut diameter. We then apply a uniaxial macroscopic strain and plot the homogenized results at various pre-charged hydrogen concentrations for both BCC and cubic cells ( $\rho_r = 20\%$ ) in Fig. 8.

The failure behavior of micro-architected materials attributes to: (1) bulk material, (2) cell architecture, and (3) relative density (porosity). Here, both BCC and cubic cells are made of same bulk material with identical relative densities ( $\rho_r = 20\%$ ), so the difference in their behavior shed light on the influence of unit-cell architecture. Although the increasing hydrogen content degrades the strength and ductility of both unit-cells, comparing macroscopic plots in Fig. 8 highlights the differences between the performance of the candidate unit-cells. At a given pre-charged hydrogen concentration, the ductility of BCC cell is higher than cubic cell, while its maximum strength is lower. The latter is more dominant in the presence of hydrogen. For example, in the absence of hydrogen ( $C_L^\infty = 0$ ), the maximum strength of BCC and cubic cells are comparable but in the presence of hydrogen at  $C_L^\infty = 0.5$ , the maximum strength

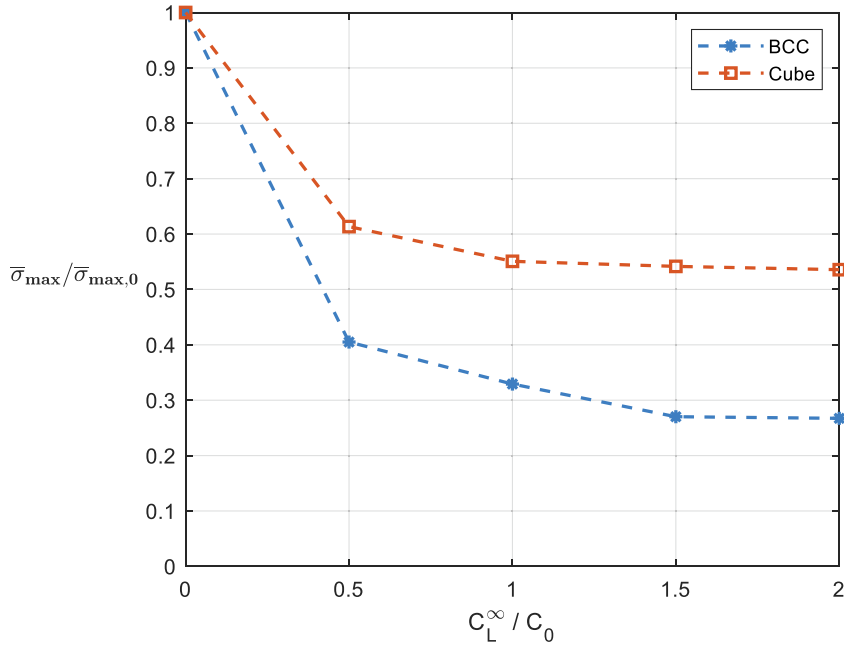


Fig. 10. Normalized failures locus of the cubic and BCC unit-cells with  $\rho_r = 20\%$  ( $C_0 = 1wppm$ ).

of the cubic cell is 1.6 times higher than the one for BCC. It is concluded that the presence of hydrogen has more detrimental effect on the strength of BCC cell. Also note that the failure mechanism changes in the presence of hydrogen. While both cubic and BCC cells have ductile behavior in the absence of hydrogen ( $C_L^\infty = 0$ ), they respectively show brittle and semi-brittle failure in the presence of hydrogen ( $C_L^\infty > 0$ ), see Fig. 8.

To better compare the behavior of unit-cells, as an example, we plot the distribution of maximum principal stress for cells with hydrogen content of  $C_L^\infty = 2.0$  in Fig. 9. We see that in both architectures the maximum stress appears at cell joints, meaning the failure initiates at these locations. Although the applied macroscopic load is identical, i.e.  $\bar{\epsilon}_{xx} = 0.3\%$ , the maximum stress level at the joints of cubic and BCC cells are 790 MPa and 2950 MPa, respectively. The higher magnitude of stresses in BCC contributes to the lower macroscopic strength levels of this unit-cell as compared to cubic cell. According to the stress-based failure criteria (discussed in Sections 3 and 4), a material point fails if its maximum principal stress exceeds the material ultimate strength. Consequently, at a given macroscopic load, more material points (elements) would fail in the BCC cell as compared to the cubic cell. Knowing that the base material and applied loads are identical, this highlights the influence of cell architecture.

As in Section 5.2, we normalize the failure loci of cubic and BCC cells by dividing the material's maximum macroscopic strength,  $\bar{\sigma}_{max}$ , by its macroscopic strength in the absence of hydrogen,  $\bar{\sigma}_{max,0}$ , see Fig. 10.

As opposed to the case in Section 5.2. where the normalized data points for different relative densities of the cubic cell lay on a single curve, here, the data points for different cell topologies—BCC and cube with same relative density—form two distinct failure loci. This implies that each micro-architected material has its own unique failure loci which depends on the unit-cell architecture. Additionally, we see the so-called saturation point is different for unit-cells, i.e. it is  $C_L^\infty = 1$  for cubic and  $C_L^\infty = 1.5$  for BCC.

Finally, we characterize the hydrogen degradation equation for a micro-architected material made of BCC unit-cell ( $\rho_r = 20\%$ ) as.

$$\frac{\bar{\sigma}_{max}}{\bar{\sigma}_{max,0}} = 0.72\exp(-3.30C_L^\infty) + 0.28 \quad (26)$$

## 6. Conclusion

We studied the role of hydrogen in strength degradation of micro-architected materials. We began by analyzing the Reynold's transport equation for hydrogen diffusion problem and obtained the governing equations for hydrogen concentration under quasi-static loading. We then used the concept of elastoplastic homogenization to bridge the scales and derive the material effective properties. We implemented these theories in a numerical scheme for decoupled diffusion-deformation analysis, in which we update the homogenization algorithm with hydrogen concentration and flow stress through UHARD subroutine and implicit formulae.

We applied the model to cubic (with  $\rho_r = 10\%$ ,  $20\%$  and  $30\%$ ) and BCC (with  $\rho_r = 20\%$ ) unit-cells along with PBC and characterized their macroscopic hydrogen degradation laws. Each micro-architected material has its unique failure loci depending on cell architecture, but one can provide a single expression to describe the behavior of a cubic unit-cell over a range of relative densities. Also, it turned out that the role of trap hydrogen in embrittlement of micro-architecture materials is negligible, especially when the base material has low ductility.

For load bearing applications and in presence of hydrogen, the cubic material outperforms the BCC because: (1) at equal hydrogen contents, its maximum strength is higher than BCC, and (2) it undergoes a less severe hydrogen degradation as compared to the BCC. On the other hand, the BCC material has higher ductility which is desirable for certain applications. Generally, micro-architected materials made of high-strength steels, e.g. AISI 4135, are prone to brittle fracture in the presence of hydrogen. This agrees with what was observed in bulk specimens, e.g. [26].

The developed computational scheme is generic and applicable to any periodic micro-architected material and is an efficient tool for assessment of hydrogen embrittlement. We proposed the design methodology and numerically characterized the macroscopic hydrogen degradation laws for cubic and BCC unit-cells. The experimental validation of the results on hydrogen embrittlement in architected materials is suggested as a part of future studies.

#### CRediT authorship contribution statement

**Danial Molavitabrzi:** Visualization, Validation, Software, Methodology, Formal analysis, Conceptualization, Writing - original draft. **Haiyang Yu:** Validation, Supervision, Software, Methodology, Formal analysis, Conceptualization, Writing - review & editing. **S. Mahmoud Mousavi:** Writing - review & editing, Validation, Supervision, Methodology, Formal analysis, Conceptualization, Funding acquisition.

#### Declaration of Competing Interest

The authors declare that they have no known competing financial interests or personal relationships that could have appeared to influence the work reported in this paper.

#### Data availability

No data was used for the research described in the article.

#### Acknowledgment

The authors D.M. and S.M.M acknowledge the financial support by the Starting Grant (2018-03636) from the Swedish Research Council (Vetenskapsrådet).

#### Appendix A

Here, we provide the details of the numerical tensile tests on uncharged notched specimens to calibrate the local maximum stress with respect to stress triaxiality (see Table A1).

We use finite element method (in Abaqus 2019) to analyze the local stresses at the vicinity of notch root for tensile bars with 0.1 mm and 0.8 mm notch radius, see [22] for other sample dimensions. We construct a 2D axisymmetric model with bilinear quadrilateral elements and only simulate one quarter of the model using symmetry boundary condition. We perform displacement-controlled numerical tensile tests by applying  $U_y$  displacement ( $U_x = UR_z = 0$ ) to a reference point which is kinematically coupled with the nodes at the top edge, see Fig. A1.

Here, we summarize the data used for material calibration in Section 3, Eq. (24).

**Table A-1**  
Local failure stress versus stress triaxiality for un-charged tensile specimens.

Sample	$\eta$	Maximum $\sigma_y$
Un-notched	0.3	1435 MPa
0.8 mm notch radius	1.15	2750 MPa
0.1 mm notch radius	1.5	3145 MPa

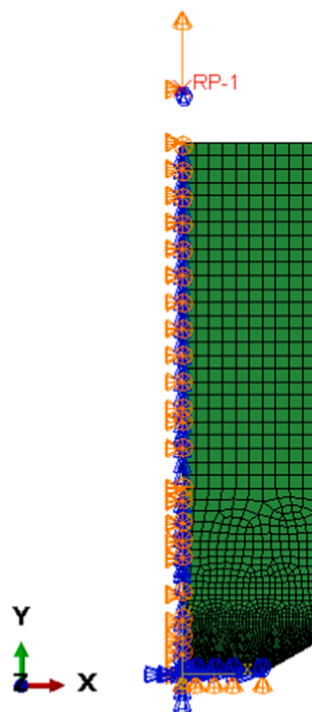


Fig. A-1. Numerical model of axisymmetric tensile sample.

## References:

- [1] L. J. Gibson and M. F. Ashby, *Cellular Solids: Structure and Properties*, 2nd ed., Cambridge: Cambridge University Press, 1997. doi: 10.1017/CBO9781139878326.
- [2] Fleck NA, Deshpande VS, Ashby MF. Micro-architected materials: past, present and future. *Proceedings of the Royal Society A: Mathematical, Physical and Engineering Sciences* Sep. 2010;466(2121):2495–516. <https://doi.org/10.1098/rspa.2010.0215>.
- [3] Dos Reis F, Ganghoffer JF. Homogenized elastoplastic response of repetitive 2D lattice truss materials. *Comput Mater Sci Mar.* 2014;84:145–55. <https://doi.org/10.1016/j.commatsci.2013.11.066>.
- [4] Molavitabrzi D, Mousavi SM. Elasticity of Anisotropic Low-Density Lattice Materials. *J Engng Mater Technol* 2020;143(021007):Nov. <https://doi.org/10.1115/1.4048931>.
- [5] Telgen B, Sigmund O, Kochmann DM. Topology Optimization of Graded Truss Lattices Based on On-the-Fly Homogenization. *J. Appl. Mech.* 2022;89(6). <https://doi.org/10.1115/1.4054186>.
- [6] 'Inverting the structure–property map of truss metamaterials by deep learning | PNAS'. <https://www.pnas.org/doi/10.1073/pnas.2111505119> (accessed Apr. 13, 2022).
- [7] Schaedler TA, et al. Ultralight Metallic Microlattices. *Science* Nov. 2011;334(6058):962–5. <https://doi.org/10.1126/science.1211649>.
- [8] Alaña M, Cutolo A, Ruiz de Galarreta S, Van Hooreweder B. Influence of relative density on quasi-static and fatigue failure of lattice structures in Ti6Al4V produced by laser powder bed fusion. *Sci Rep* Sep. 2021;11(1):19314. <https://doi.org/10.1038/s41598-021-98631-3>.
- [9] Großmann A, Gosmann J, Mittelstedt C. Lightweight lattice structures in selective laser melting: Design, fabrication and mechanical properties. *Mater Sci Engng, A* Oct. 2019;766:138356. <https://doi.org/10.1016/j.msea.2019.138356>.
- [10] Hammetter CI, Rinaldi RG, Zok FW. Pyramidal Lattice Structures for High Strength and Energy Absorption. *J. Appl. Mech.* 2013;80(4). <https://doi.org/10.1115/1.4007865>.
- [11] Li P, Ma YE, Sun W, Qian X, Zhang W, Wang Z. Fracture and failure behavior of additive manufactured Ti6Al4V lattice structures under compressive load. *Engng Fract Mech Mar.* 2021;244:107537. <https://doi.org/10.1016/j.engfracmech.2021.107537>.
- [12] Molavitabrzi D, Ekberg A, Mousavi SM. Computational model for low cycle fatigue analysis of lattice materials: Incorporating theory of critical distance with elastoplastic homogenization. *Eur J Mech A Solids Mar.* 2022;92:104480. <https://doi.org/10.1016/j.euromechsol.2021.104480>.
- [13] Drücker S, et al. Experimental and numerical mechanical characterization of additively manufactured Ti6Al4V lattice structures considering progressive damage. *Int J Mech Sci Jan.* 2021;189:105986. <https://doi.org/10.1016/j.ijmecsci.2020.105986>.
- [14] Seiler PE, Li K, Deshpande VS, Fleck NA. The Influence of Strut Waviness on the Tensile Response of Lattice Materials. *J Appl Mech* 2020;88(031011):Dec. <https://doi.org/10.1115/1.4049140>.
- [15] Geng X, Lu Y, Liu C, Li W, Yue Z. Fracture characteristic analysis of cellular lattice structures under tensile load. *Int J Solids Struct* May 2019;163:170–7. <https://doi.org/10.1016/j.ijsolstr.2019.01.006>.
- [16] Molavitabrzi D, Bengtsson R, Botero C, Rännar L-E, Mahmoud Mousavi S. Damage-induced failure analysis of additively manufactured lattice materials under uniaxial and multiaxial tension. *Int. J. Solids Struct.* 2022;252:111783. <https://doi.org/10.1016/j.ijsolstr.2022.111783>.
- [17] Boniotti L, Dancette S, Gavazzoni M, Lachambre J, Buffiere JY, Foletti S. Experimental and numerical investigation on fatigue damage in micro-lattice materials by Digital Volume Correlation and  $\mu$  CT-based finite element models. *Engng Fract Mech* May 2022;266:108370. <https://doi.org/10.1016/j.engfracmech.2022.108370>.
- [18] Liu L, Kamm P, García-Moreno F, Banhart J, Pasini D. Elastic and failure response of imperfect three-dimensional metallic lattices: the role of geometric defects induced by Selective Laser Melting. *J Mech Phys Solids* Oct. 2017;107:160–84. <https://doi.org/10.1016/j.jmps.2017.07.003>.
- [19] Gross A, Pantidis P, Bertoldi K, Gerasimidis S. Correlation between topology and elastic properties of imperfect truss-lattice materials. *J Mech Phys Solids Mar.* 2019;124:577–98. <https://doi.org/10.1016/j.jmps.2018.11.007>.
- [20] Moussa A, Melancon D, El Elmi A, Pasini D. Topology optimization of imperfect lattice materials built with process-induced defects via Powder Bed Fusion. *Addit Manuf Jan.* 2021;37:101608. <https://doi.org/10.1016/j.addma.2020.101608>.

- [21] Ossola E, Shapiro AA, Pate A, Firdosy S, Brusa E, Sesana R. Fabrication defects and limitations of AlSi10Mg lattice structures manufactured by selective laser melting. Proceedings of the Institution of Mechanical Engineers, Part L: Journal of Materials: Design and Applications Oct. 2021;235(9):2071–82. <https://doi.org/10.1177/14644207211012726>.
- [22] Ayas C, Deshpande VS, Fleck NA. A fracture criterion for the notch strength of high strength steels in the presence of hydrogen. J Mech Phys Solids Feb. 2014;63:80–93. <https://doi.org/10.1016/j.jmps.2013.10.002>.
- [23] Barrera O, Tarleton E, Tang HW, Cocks ACF. Modelling the coupling between hydrogen diffusion and the mechanical behaviour of metals. Comput Mater Sci Sep. 2016;122:219–28. <https://doi.org/10.1016/j.commatsci.2016.05.030>.
- [24] Yu H, Olsen JS, Alvaro A, Olden V, He J, Zhang Z. A uniform hydrogen degradation law for high strength steels. Engng Fract Mech May 2016;157:56–71. <https://doi.org/10.1016/j.engfracmech.2016.02.001>.
- [25] Ahn DC, Sofronis P, Dodds RH. On hydrogen-induced plastic flow localization during void growth and coalescence. Int J Hydrogen Energy Nov. 2007;32(16):3734–42. <https://doi.org/10.1016/j.ijhydene.2006.08.047>.
- [26] Wang M, Akiyama E, Tsuzaki K. Effect of hydrogen on the fracture behavior of high strength steel during slow strain rate test. Corros Sci Nov. 2007;49(11):4081–97. <https://doi.org/10.1016/j.corsci.2007.03.038>.
- [27] Wang M, Akiyama E, Tsuzaki K. Determination of the critical hydrogen concentration for delayed fracture of high strength steel by constant load test and numerical calculation. Corros Sci Aug. 2006;48(8):2189–202. <https://doi.org/10.1016/j.corsci.2005.07.010>.
- [28] Bertsch KM, Nagao A, Rankouhi B, Kuehl B, Thoma DJ. Hydrogen embrittlement of additively manufactured austenitic stainless steel 316 L. Corros Sci Nov. 2021;192:109790. <https://doi.org/10.1016/j.corsci.2021.109790>.
- [29] Strakosova A, Roudnická M, Ekrt O, Vojtěch D, Michalčová A. Hydrogen Embrittlement of the Additively Manufactured High-Strength X3NiCoMoTi 18–9–5 Maraging Steel. Materials Sep. 2021;14(17):5073. <https://doi.org/10.3390/ma14175073>.
- [30] Sung S-J, Pan J, Korinko PS, Morgan M, McWilliams A. Simulations of fracture tests of uncharged and hydrogen-charged additively manufactured 304 stainless steel specimens using cohesive zone modeling. Engng Fract Mech Mar. 2019;209:125–46. <https://doi.org/10.1016/j.engfracmech.2019.01.006>.
- [31] Oriani RA. The diffusion and trapping of hydrogen in steel. Acta Metall Jan. 1970;18(1):147–57. [https://doi.org/10.1016/0001-6160\(70\)90078-7](https://doi.org/10.1016/0001-6160(70)90078-7).
- [32] Tabata T, Birnbaum HK. Direct observations of the effect of hydrogen on the behavior of dislocations in iron. Scr Metall Jul. 1983;17(7):947–50. [https://doi.org/10.1016/0036-9748\(83\)90268-5](https://doi.org/10.1016/0036-9748(83)90268-5).
- [33] Sofronis P, Liang Y, Aravas N. Hydrogen induced shear localization of the plastic flow in metals and alloys. Eur J Mech A Solids Nov. 2001;20(6):857–72. [https://doi.org/10.1016/S0997-7538\(01\)01179-2](https://doi.org/10.1016/S0997-7538(01)01179-2).
- [34] Liang Y, Sofronis P, Aravas N. On the effect of hydrogen on plastic instabilities in metals. Acta Mater May 2003;51(9):2717–30. [https://doi.org/10.1016/S1359-6454\(03\)00081-8](https://doi.org/10.1016/S1359-6454(03)00081-8).
- [35] Yvonnet J. Computational Homogenization of Heterogeneous Materials with Finite Elements. Springer International Publishing 2019. <https://doi.org/10.1007/978-3-030-18383-7>.
- [36] D. Gross and T. Seelig, Fracture Mechanics: With an Introduction to Micromechanics, 3rd ed. Springer International Publishing, 2018. doi: 10.1007/978-3-319-71090-7.
- [37] Bai Y, Wierzbicki T. A new model of metal plasticity and fracture with pressure and Lode dependence. Int J Plast Jun. 2008;24(6):1071–96. <https://doi.org/10.1016/j.ijplas.2007.09.004>.
- [38] Bai Y, Teng X, Wierzbicki T. On the Application of Stress Triaxiality Formula for Plane Strain Fracture Testing. J. Engng. Mater. Technol. Mar. 2009;131(2). <https://doi.org/10.1115/1.3078390>.
- [39] Darlet A, Desmorat R. Stress triaxiality and Lode angle along surfaces of elastoplastic structures. Int J Solids Struct Aug. 2015;67–68:71–83. <https://doi.org/10.1016/j.ijsolstr.2015.03.006>.
- [40] Fernández-Sousa R, Betegón C, Martínez-Pañeda E. Analysis of the influence of microstructural traps on hydrogen assisted fatigue. Acta Mater Oct. 2020;199:253–63. <https://doi.org/10.1016/j.actamat.2020.08.030>.